Microscopic structural relaxation in a sheared supercooled colloidal liquid

Dandan Chen,[1,*] Denis Semwogerere,[1] Jun Sato,[2] Victor Breedveld,[2] and Eric R. Weeks[1]

[1]*Department of Physics, Emory University, Atlanta, Georgia 30322, USA*
[2]*School of Chemical and Biomolecular Engineering, Georgia Institute of Technology,*
311 Ferst Drive NW, Atlanta, Georgia 30332-0100, USA

The rheology of dense amorphous materials under large shear strain is not fully understood, partly due to the difficulty of directly viewing the microscopic details of such materials. We use a colloidal suspension to simulate amorphous materials and study the shear-induced structural relaxation with fast confocal microscopy. We quantify the plastic rearrangements of the particles in several ways. Each of these measures of plasticity reveals spatially heterogeneous dynamics, with localized regions where many particles are strongly rearranging by these measures. We examine the shapes of these regions and find them to be essentially isotropic, with no alignment in any particular direction. Furthermore, individual particles are equally likely to move in any direction other than the overall bias imposed by the strain.

I. INTRODUCTION

Many common materials have an amorphous structure, such as shaving cream, ketchup, toothpaste, gels, and window glass [1–4]. In some situations, these are viscous liquids, for example, when window glass is heated above the glass transition temperature or a shaving cream foam that has been diluted by water to become a liquid with bubbles in it. In other situations, these are viscoelastic or elastic solids, such as gels and solid window glass [5]. For solidlike behavior, when a small stress is applied, the materials maintain their own shapes; at larger stresses above the yield stress, they will start to flow [6–8]. Understanding how these materials yield and flow is important for the processing of these materials and understanding their strength in the solid state [9–11].

A particularly interesting system to study is a colloidal suspension. These consist of micron- or submicron-sized solid particles in a liquid. At high particle concentration, macroscopically, these are pastes and thus of practical relevance [6]. Additionally, for particles with simple hard-sphere-like interactions, colloidal suspensions also serve as useful model systems of liquids, crystals, and glasses [12–15]. Such colloidal model systems have the advantage that they can be directly observed with microscopy [16–18]. Our particular interest in this paper is using colloidal suspensions to model supercooled and glassy materials. The control parameter for hard-sphere systems is the concentration, expressed as the volume fraction ϕ, and the system acts like a glass for $\phi > \phi_g \approx 0.58$. The transition is the point where particles no longer diffuse through the sample; for $\phi < \phi_g$, spheres do diffuse at long times, although the asymptotic diffusion coefficient D_∞ decreases sharply as the concentration increases [19–21]. The transition at ϕ_g occurs even though the spheres are not completely packed together; in fact, the density must be increased to $\phi_{RCP} \approx 0.64$ for "random-close-packed" spheres [22–26] before the spheres

are motionless. Prior work has shown remarkable similarities between colloidal suspensions and conventional molecular glasses [12,19,27–33].

One important unsolved problem related to amorphous materials is to understand the origin of their unique rheological behavior under shear flow. Early in the 1970s, theory predicted the existence of "flow defects" beyond yielding [9], later termed shear transformation zones (STZ) [34]. These microscopic motions result in plastic deformation of the sheared samples [35,36]. Simulations later found STZs by examining the microscopic local particle motions [11,37,38]. Recently, fast confocal microscopy has been used to examine the shear of colloidal suspensions [39] and STZs have been directly observed [15]. This provided direct evidence to support theoretical work on STZs [9,34,40,41].

However, questions still remain. First, most of the prior work has focused on the densest possible samples at concentrations which are glassy ($\phi > \phi_G$) [15,39]. Given that the macroscopic viscosity of colloidal suspensions changes dramatically near and above ϕ_G [42], it is of interest to study slightly less dense suspensions under shear, for which rearrangements might be easier [43]. In this paper, we present such results. Second, prior investigations of sheared amorphous materials have used a variety of different ways to quantify plastic deformation [15,39,44,45]. In this paper, we will compare and contrast plastic deformations defined in several different ways. While they do capture different aspects of plastic deformation, we find that some results are universal. In particular, in a sheared suspension, there are three distinct directions: the strain velocity, the velocity gradient, and the direction mutually perpendicular to the first two (the "vorticity" direction). We find that plastic deformations are isotropic with respect to these three directions, apart from the trivial anisotropy due to the velocity gradient. The deformations are both isotropic in the sense of individual particle motions and in the sense of the shape of regions of rearranging particles.

II. EXPERIMENTAL METHODS

The experimental setup of our shear cell is shown in Fig. 1 and is similar to that described in Refs. [39,46]. The glass
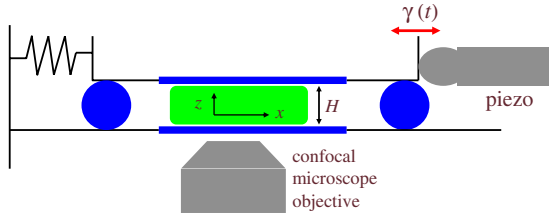
*dchen@physics.emory.edu

FIG. 1. (Color online) Sketch of the shear cell. A fluorescent sample (gray, green) is put between two parallel glass plates (dark gray, blue) with gap H set by three ball bearings, two of which are shown. The top plate is movable, controlled by a piezomotor driven by a triangular wave. The bottom plate is fixed and the confocal microscope takes images from underneath. Note the definition of the coordinate system, where x is in the velocity direction and z is in the velocity gradient direction.

plates are 15 mm in diameter and to the top plate is glued a small piece of glass with dimensions 5×1 mm^2, with the long dimension oriented in the direction of motion x. The purpose of this piece of glass is to decrease the effective gap size. Between the plates are three ball bearings used to control the gap size; for all of our data, we maintain a gap size of $H = 130$ μm. Over the 5 mm length of the small pieces of glass, the gap varies by no more than 15 μm; over the narrower dimension of the small pieces of glass, the gap varies by no more than 10 μm. Thus, overall, the sample is between two plates which are parallel to within 1% and in the direction of shear, they are parallel to within 0.3%.

A droplet of the sample (volume $\sim$200 μl) is placed between the two pieces of glass. The top plate is free to move in the x direction and the bottom plate is motionless. The shear rate is controlled by a piezoelectric actuator (Piezomechanik GmbH Co.) driven by a triangular wave signal with a period ranging from $T = 150$ to 450 s and an amplitude of $A = 175$ μm. Thus we achieve strains of $\gamma_0 = A/H = 1.4$. Prior to taking data, we allow the shear cell to go through at least one complete period, but usually not more than three complete periods.

Our samples (Fig. 2) are poly(methyl methacrylate) colloids sterically stabilized with poly-12-hydroxystearic acid [47]. These particles are suspended in a mixture of 85% cyclohexybromide and 15% decalin by weight. This mixture matches both the density and the index of refraction of the particles. To visualize the particles, they are dyed with rhodamine 6G [48]. The particles have a radius $a = 1.05 \pm 0.04$ μm, with the error bar indicating the uncertainty in the mean diameter; additionally, the particles have a polydispersity of no more than 5% (as these particles can crystallize fairly easily) [12,49–51].

In this work we study several samples with volume fractions ϕ between 0.51 and 0.57. Thus, our samples are quite dense liquids, comparable to prior work with "supercooled" colloidal liquids [12,43]. The differences in volume fraction between samples are certain to within $\pm$0.01 and the absolute volume fraction has a systematic uncertainty of $\pm$0.06 due to the uncertainty of the particle radius a. However, none of our samples appear glassy and thus we are confident our maximum volume fraction is less than $\sim$0.6. While the particles in decalin behave as hard spheres, in our solvent mix-
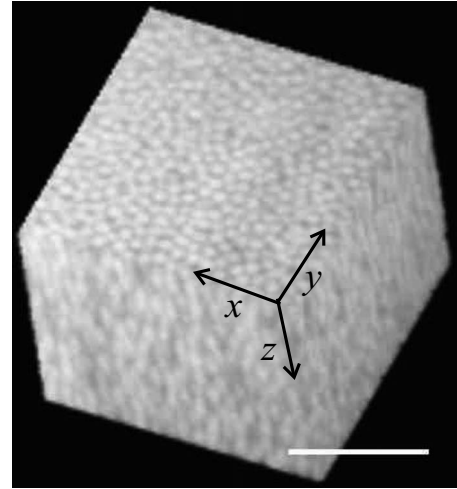

FIG. 2. A $20 \times 20 \times 20$ μm^3 image of a supercooled colloidal liquid taken 15 μm away from the fixed bottom plate by our confocal microscope in less than 1 s. Scale bar represents 10 μm.

ture, they carry a slight charge. This does not seem to affect the phase behavior dramatically at high volume fractions such as what we consider in this work (see, for example, [52,53]).

To characterize the relative importance of Brownian motion and the imposed strain field, we can compute the modified Peclet number, Pe$^\star = \dot{\gamma} a^2/2D_\infty$, where D_∞ is the long-time diffusion coefficient of the quiescent sample. We measure D_∞ from mean-square displacement data taken from the quiescent sample with the same volume fraction. The large Δt data for the mean-square displacement can be fit using $\langle \Delta x^2 \rangle = 2D_\infty \Delta t$. Roughly, $a^2/2D_\infty$ reflects the average duration a particle is caged by its neighbors in the dense suspension.

$\dot{\gamma}$ is the imposed strain rate $2A/(HT)$ and a is the particle size. The extra factor of 2 in $\dot{\gamma}$ is because we use a triangle wave and thus the half period sets the strain rate. For our samples, we find $D_\infty \approx 5 \times 10^{-4}$ μm^2/s and we have $\dot{\gamma}$ ranging from 0.0060 to 0.0180 s^{-1}; thus Pe$^\star \approx 7$–20. Given that Pe$^\star > 1$, the implication is that the motions we will observe are primarily caused by the strain rather than due to Brownian motion. We use the modified Peclet number based on D_∞ rather than the bare Peclet number based on the dilute-limit diffusivity D_0, as we will focus our attention on the dynamics at long time scales, which we will show are indeed shear induced.

Shear-induced crystallization has been found in previous work [54,55]. As we wish to focus on the case of sheared amorphous materials, we check our data to look for crystalline regions using standard methods which detect ordering [52,53,56–58]. Using these methods, we find that particles in apparently crystalline regions comprise less than 3% of the particles in each of our experiments and are not clustered, suggesting that the apparently crystalline regions are tiny. This confirms that our samples maintain amorphous structure over the time scale of our experiments, although perhaps if we continued the shearing over many more cycles, we would find shear-induced crystallization.

We use a confocal microscope to image our sample (the "VT-Eye," Visitech) using a 100$\times$ oil lens (numerical

aperture=1.40) [17,48,59]. A three-dimensional (3D) image with a volume $50 \times 50 \times 20$ μm^3 is acquired in less than 2 s; these images contain about 6000 particles. The 3D image is $256 \times 256 \times 100$ pixels, so approximately 0.2 μm per pixel in each direction. Figure 2 shows a representative image from a somewhat smaller volume. The 2 s acquisition time is several orders of magnitude faster than the diffusion for particles in our high volume fraction sample. To avoid any boundary effects [60], we scan a volume at least 20 μm away from the bottom plate. Particle positions are determined with an accuracy of 0.05 μm in x and y and 0.1 μm in z. This is done by first spatially filtering the 3D image with a bandpass filter designed to remove noise at high and low spatial frequencies and then looking for local maxima in the image intensity [61]. Our tracking algorithm is similar to prior work [48,61,62], where we first identify particles within each 3D image, next remove the overall average shear-induced motion from all of the particles, then track the particles in the "coshearing" reference frame using conventional techniques [61], and finally add back in the shear-induced motion that was previously removed. This is similar to the "iterated Crocker-Grier tracking" method described in Ref. [62]. The key idea of this tracking is that particles should not move more than an interparticle spacing between each image; this condition is satisfied in the coshearing reference frame.

Due to the strain, particles that start near one face of the imaging volume are carried outside the field of view, while on the opposite face, new particles are brought inside. Thus, for larger strains, the total number of particles viewed for the entire duration diminishes. For the data discussed in this work, we consider both instantaneous quantities and quantities averaged over the entire half cycle of strain. For the former, we view ~5500 particles, while for the latter, we typically can follow ~3000 particles, which limits our statistics slightly.

III. RESULTS

A. Locally observed strain

Our goal is to understand if the local shear-induced motion is isotropic in character. However, first we seek to understand and quantify the more global response of our sheared samples.

When shearing disordered materials or complex fluids, one often finds shear localization or shear banding due to the nonlinear yielding and relaxation in local regions [6,7,63,64]. To check for this in our data, we start by taking 3D images under the applied shear rate $\dot{\gamma}_{macro}$=0.016 s^{-1} over a very large range in z, from 0 to 70 μm away from the bottom plate, almost half of the gap between two shearing plates. To allow us to visualize more clearly over such a large depth, we dilute the dye concentration by mixing dyed and undyed colloids at a number ratio of around 1:80 and keeping the desired volume fraction $\phi \approx 0.50$. Our sample does indeed form a shear band, as shown in Fig. 3, which shows the particle velocity v_x in the direction of the shear as a function of the depth z. The velocity changes rapidly with z in the range $0 < z < 20$ μm and then more slowly for $z > 20$ μm;
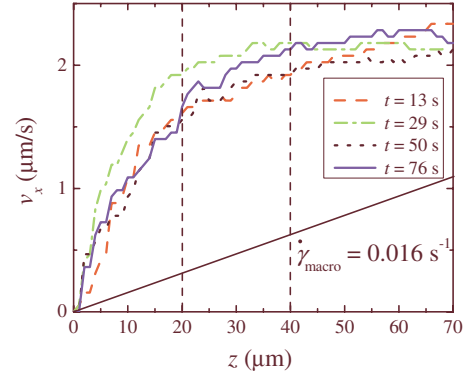

FIG. 3. (Color online) Shear profile $v_x(z)$ within a $50 \times 50 \times 70$ μm^3 volume, measured at different times during one half period $T/2$=84 s. The total macroscopic strain applied in 84 s is 1.35. The sample has a volume fraction $\phi \approx 0.50$ and the global applied shear rate is $\dot{\gamma}_{macro}$=0.016 s^{-1} controlled by the piezomotor. If there was not a shear band, one would expect to observe a linear velocity profile as indicated by the lower thick diagonal line. The four curves represent different times during the half period as indicated. Note that these data are obtained using a coarse-grained image velocimetry method [62] rather than particle tracking. Here we take rapid images over the full volume with a spacing of z=1 μm in the vertical direction. For each value of z, we cross correlate subsequent images to obtain a mean instantaneous velocity v_x with a resolution of 0.05 μm/s, set by the pixel size and the time between images (see Ref. [62] for further details).

thus, much of the shear occurs adjacent to the stationary plate at z=0 μm, similar to prior work which found shear adjacent to one of the walls [6,7,63–65]. Furthermore, the velocity profile is relatively stable during the course of the half period, as seen by the agreement between the velocity profiles taken at different times during this half period (different lines in Fig. 3). Thus, the shear band develops quickly inside the supercooled colloidal liquid and remains fairly steady under the constant applied strain rate. The location and size of the shear band vary from experiment to experiment.

Given the existence of a shear band, the applied strain is not always the local strain. In this work, we wish to focus on the motion induced by a local strain rather than the global formation of shear bands. Thus, for all data sets presented below, we always calculate the local instantaneous strain rate $\dot{\gamma}_{meso}(t) = \frac{v_x(z+\Delta z, t) - v_x(z, t)}{\Delta z}$. Here, Δz=20 μm is the height of the imaged volume. Related to $\dot{\gamma}_{meso}$, we can calculate the total local applied strain by integrating $\dot{\gamma}_{meso}(t)$,

$$\gamma_{meso}(t) = \int_0^t \dot{\gamma}_{meso}(t') dt'. \qquad (1)$$

Furthermore, we verify that for each data set considered below, $v_x(z)$ varies linearly with z within the experimental uncertainty and thus $\dot{\gamma}_{meso}$ is well defined even if globally it varies (Fig. 3).

While the shape of the shear band is essentially constant (Fig. 3), in many cases the local strain rate varies slightly with time. As our forcing is a triangle wave, over any given
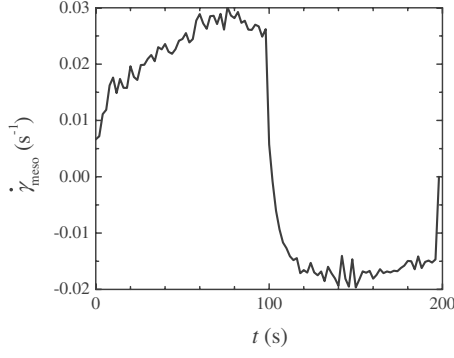
FIG. 4. Typical example of a measured local instantaneous shear rate over one period of shearing in a gap of 20–40 μm away from the fixed bottom plate. The sample has volume fraction $\phi=0.51$, the applied strain rate is $\dot{\gamma}_{macro}=0.013$ s^{-1}, and the period is $T=200$ s.

half cycle the global applied strain rate is a constant. We can measure the local strain rate for each data set; a typical example is shown in Fig. 4. This figure shows the local instantaneous measured strain rate within the region 20 μm$<z$ <40 μm over one full period. After the shearing starts, $\dot{\gamma}_{meso}$ quickly rises up to 0.015 s^{-1}, implying that the shear band has formed. Subsequently, the local strain rate continues to increase up to 0.030 s^{-1} over the rest of the half period. The small fluctuations of $\dot{\gamma}_{meso}$ are due to the microscopic rearrangements of particles, which can be somewhat intermittent. Given that the local instantaneous strain rate is not constant (despite the constant applied strain rate), we will characterize our data sets by the time-averaged local strain rate defined as

$$\bar{\dot{\gamma}}_{meso} = \frac{\gamma_{meso}(t)}{t}, \qquad (2)$$

typically using $t=T/2$, the half period of the strain. That is, we consider $\bar{\dot{\gamma}}_{meso}$ as one key parameter characterizing each data set, although we will show that we see little dependence on this parameter. In the rest of the paper, the choice $t=T/2$ will be assumed, except where noted when we wish to characterize the mesoscopic strain for time scales shorter than $T/2$.

At this point, we have defined the key control parameters, which are measured from each experimental data set: the strain rate $\bar{\dot{\gamma}}_{meso}$ and the strain amplitude γ_{meso}. We next consider how these variables relate to the magnitude of the shear-induced particle motion.

B. Individual particle motions

Because of our large local strains (measured to be γ_{meso} >0.3 for all cases), we observe significant particle motion, as shown Figs. 5(a) and 5(b). In the laboratory reference frame, the microscopic velocity gradient is obvious either in the raw trajectories [Fig. 5(a)] or in the large displacements [Fig. 5(b)] measured between the beginning and end of the half period. However, in a sense, much of this motion is "trivial;" we wish to observe what nontrivial local rearrange-
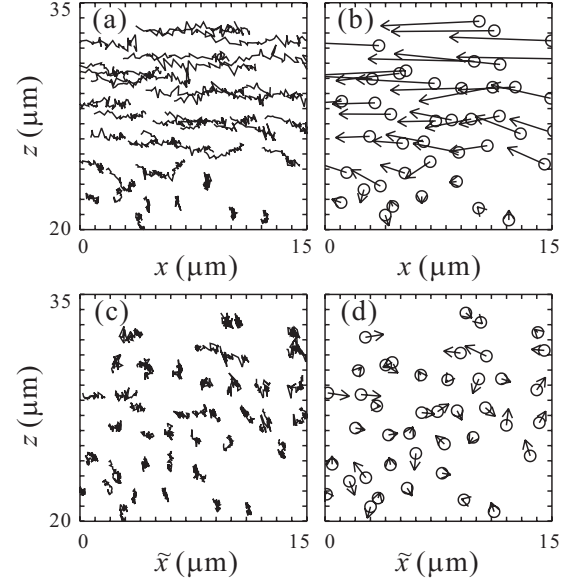

FIG. 5. Trajectories of colloids in an xz slice (5 μm thick in the y direction) (see Fig. 1 for the coordinate axes). The sample has $\phi=0.51$ and the data shown correspond to a locally measured accumulated strain $\gamma_{meso}=0.43$ over 45 s of data, so the effective strain rate is $\bar{\dot{\gamma}}_{meso}=\gamma_{meso}/\Delta t=0.0096$ s^{-1}. (a) Trajectories in a reference frame comoving with the average velocity $v_x(z=20$ μm). (b) Displacements corresponding to data from panel (a), where the start point of each particle is marked with a circle and the end point is marked with an arrowhead. (c) The same data, but with the affine motion removed; this is the $\tilde{x}z$ plane. (d) Displacements corresponding to panel (c).

ments are caused by the strain. To do this, we consider the nonaffine motion by removing averaged particle displacements at the same depth z from the real trajectories of particles [38,39,44,66,67]

$$\tilde{x}_i(t) = x_i(t) - \int_0^t \dot{\gamma}_{meso}(t')z_i(t')dt', \qquad (3)$$

where the removed integral represents the shearing history of the particle i. To be clear, the shearing history is based on the average motion within the entire imaged region and the remaining motion of particle i is caused by interactions with neighboring particles due to the shear. This motion is shown in Fig. 5(c), showing the $\tilde{x}z$ plane rather than the xz plane; the particles move shorter distances. Their overall displacements in this "desheared" reference frame are shown in Fig. 5(d). A few trajectories are up to 2 μm long, comparable to the particle diameter. These nonaffine displacements shown in Fig. 5(d) are much smaller than the raw displacements of Fig. 5(b), but much larger than thermally activated Brownian motion, which takes more than 1000 s to diffuse over a 1 μm distance in our dense samples (comparable to the particle radius a). These nonaffine motions $\tilde{x}$ reflect shear-induced plastic changes inside the structure.

To quantify the amount of this nonaffine motion $\tilde{x}$, one could calculate the mean-squared displacements (MSD) often defined as
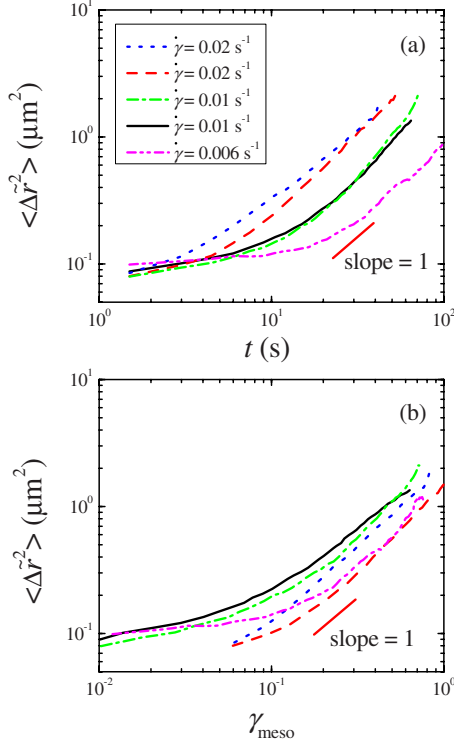
FIG. 6. (Color online) (a) Mean-square displacement of the non-affine motion $\Delta\tilde{r}$ as a function of the time t since the start of shear. (b) The same data plotted as a function of the accumulated strain $\gamma_{\text{meso}} = \int_0^t \dot{\gamma}_{\text{meso}}(t')dt'$. The five curves represent five data sets with the same volume fraction $\phi = 0.51$ but three different shear rates $\bar{\dot{\gamma}}_{\text{meso}}$ as indicated in the figure. The total accumulated strain is the final point reached by each curve in panel (b).

$$\langle\Delta\tilde{x}^2\rangle(\Delta t) = \langle[\tilde{x}_i(t+\Delta t) - \tilde{x}_i(t)]^2\rangle_{i,t} \quad (4)$$

where the angle brackets indicate an average over time t as well as particles i. Thus, this identity assumes that environmental conditions remain the same for all the time since it does not depend on t. However, as shown by Fig. 4, the shear rate $\dot{\gamma}_{\text{local}}(t)$ depends on the time. Therefore, we use an alternate formulation

$$\langle\Delta\tilde{x}^2\rangle(t) = \langle[\tilde{x}_i(t) - \tilde{x}_i(t=0)]^2\rangle_i, \quad (5)$$

where the angle brackets only indicate an average over particles and t is the time since the start of a half period of shear. Figure 6(a) shows mean squared displacement (MSD) of the nonaffine motion $\Delta\tilde{r}^2 = \Delta\tilde{x}^2 + \Delta y^2 + \Delta z^2$ as a function of t for five different experiments with different strain rates $\bar{\dot{\gamma}}_{\text{meso}}$, from 0.02 to 0.006 s^{-1}. In each case, the curves nearly reach a slope of 1 on the log-log plot, indicating that shear quickly facilitates particles' rearrangements. The magnitude of the motion is $\Delta\tilde{r}^2 \approx 1$ μm^2, indicating that the original structure is mostly lost [68].

Figure 6(a) also shows that $\Delta\tilde{r}^2$ is larger for faster strain rates at the same t. We find that this motion is determined by the accumulated strain, as shown in Fig. 6(b), by replotting the MSD as a function of γ_{meso} [Eq. (1)]. In this graph, the
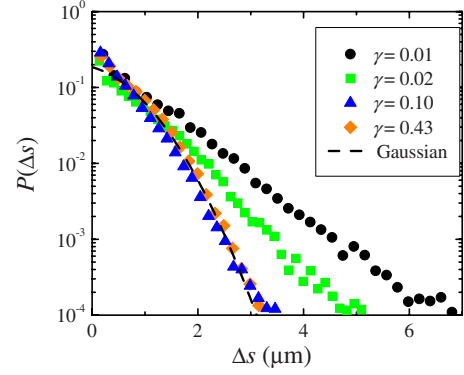

FIG. 7. (Color online) Probability distribution function of $\Delta s = \Delta\tilde{r}/\gamma_{\text{meso}}^{0.5}$, the nonaffine displacement $\Delta\tilde{r}$ scaled by the local strain $\gamma_{\text{meso}}^{0.5}$. Data shown are from one experimental run using portions of the data corresponding to strain increments $\gamma_{\text{meso}} = 0.01$, 0.02, 0.10, and 0.43. These correspond to time intervals $\Delta t = 1.5$, 4.5, 16.5, and 45 s. $P(\Delta s)$ is normalized so that the integral over all vectors $\Delta\vec{s}$ is equal to 1, similar to Ref. [67]. For small strains, the curves have large exponential tails and for larger strain, the tails become smaller and appear more Gaussian. Dashed line is Gaussian fit for $\gamma_{\text{meso}} = 0.43$. For this sample, data and parameters are the same as Fig. 5.

curves are grouped closer together and there is no obvious dependence on $\bar{\gamma}_{\text{meso}}$.

It suggests that the accumulated strain is an important parameter in the structural relaxation, which was also found in previous work on shear transformation zones [67,69] and is similar behavior to that seen for athermal sheared systems [70]. Additionally, Fig. 6(b) shows that the slopes of the curves are close to 1 when $\gamma_{\text{meso}} > 0.1$, confirming that the accumulated strain in our experiments is large enough to rearrange the original structure in a supercooled colloidal liquid. We stress that the rough agreement between the curves seen in Fig. 6(b) is based on the locally measured applied strain and not the macroscopically applied strain.

An earlier study of steady shear applied to colloidal glasses by Besseling *et al.* [39] found that the diffusion time scale τ scaled as $\dot{\gamma}^{-0.8}$ and simulations also found power-law scaling [37,38]. The collapse of our MSD curves [Fig. 6(b)] seems to imply $\tau \sim \dot{\gamma}^{-1.0}$. It is possible that the disagreement between these results is too slight to be clear over our limited range in $\dot{\gamma}$ (less than 1 decade). Also, we study supercooled fluids whereas Ref. [39] examines colloidal glasses. Furthermore, our maximum local strain is $\gamma_{\text{meso}} = 1.6$, while Ref. [39] considers steady strain up to a total accumulated strain of 10. Another recent study of sheared colloidal glasses [71] implies a result similar to ours, $\tau \sim \dot{\gamma}^{-1.0}$, but did not discuss the apparent difference with Ref. [39].

To better understand the mean-square displacement curves (Fig. 6), we wish to examine the data being averaged to make these curves. We do so by plotting the distributions of displacements $\Delta\tilde{r}$ in Fig. 7. To better compare the shapes of these distributions, we normalize these displacements by the strain and thus plot $P(\Delta s)$, where $\Delta s \equiv \Delta\tilde{r}/(\gamma_{\text{meso}}^{0.5})$; this normalization is motivated by the observation that at large γ_{meso}, we have $\langle\Delta\tilde{r}^2\rangle \sim \gamma_{\text{meso}}$ (Fig. 6) [67]. Furthermore, we normalize $P(\Delta s)$ so that the integral over all vectors $\Delta\vec{s}$ is equal to 1, similar to Ref. [67]. Figure 7 shows that the
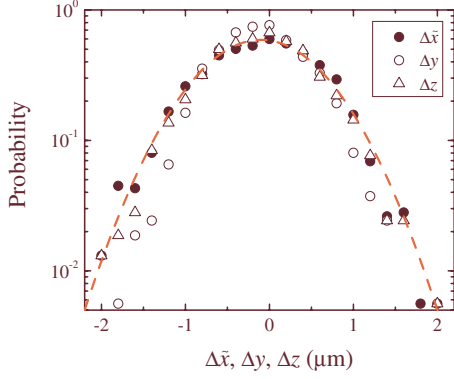
FIG. 8. (Color online) Probability distribution functions for non-affine motions in each direction, $\Delta \tilde{x}$ (filled cycle), Δy (hollow circle), and Δz (hollow triangle). Red curve is a Gaussian fit to the $\Delta \tilde{x}$ data. For this sample, parameters are the same as Fig. 5 (ϕ =0.51, γ_{meso}=0.43, $\bar{\tilde{\gamma}}_{meso}$=0.0096 s^{-1}, Δt=45 s).

distributions corresponding to small strains are much broader than those corresponding to large strains. For the smallest strain, the distribution has a large exponential tail over 3 orders of magnitude. For larger strains ($\gamma_{meso}>0.1$), the curves are no longer exponential and the tails are shorter, indicating fewer extreme events. These curves appear more like Gaussian distributions. At the larger strain values ($\gamma_{meso}>0.1$), the distributions collapse; this is the same strain regime for which the mean-square displacement becomes linear with γ_{meso} [Fig. 6(b)]. As Ref. [67] suggests, the exponential tail for small strains is similar to what has been seen for individual plastic events [66,72], while the distributions for larger strains are consistent with successive temporally uncorrelated plastic events drawn from the exponential distribution. However, it is possible that these events are spatially correlated, which will be seen below.

The mean-square displacement data we have shown (Fig. 6) treat all three directions equivalently, with the exception that the x displacements have had their nonaffine motions removed. However, the three directions are not equivalent physically: the x direction corresponds to the shear-induced velocity, the y direction is the vorticity direction, and z is the velocity gradient direction. To look for differences in motion between these three directions, we plot the probability distribution of the displacements [$\Delta \tilde{x}, \Delta y, \Delta z$] in Fig. 8. The three distributions agree with each other and in fact are symmetric around the origin. This suggests that the shear-induced motions are isotropic. Furthermore, they are well-fit by a Gaussian, suggesting that the shear-induced motion liquefies the sample (at least at the large γ_{meso} considered for Fig. 8). This seems natural in the context of jamming, where adding more strain moves the sample farther from the jammed state [5]. Of course, in our raw data, the Δx data show a significant bias in the direction of the shear-induced velocity; but it is striking that the nonaffine displacements $\Delta \tilde{x}$ show no difference from the displacements in y and z as also found in sheared colloidal glass [38,39].

Thus far, we have established that shear-induced particle displacements are closely tied to the total applied strain γ_{meso} [Fig. 6(b)]. We then introduced the nonaffine motion $\Delta \tilde{r}$
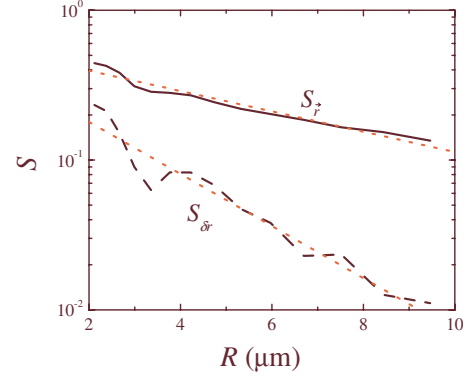

FIG. 9. (Color online) Spatial correlation functions $S_{\tilde{r}}$ and $S_{\delta r}$ characterizing particle motion. Data are the same as Fig. 5 (ϕ =0.51, γ_{meso}=0.43 over 45 s of data, and $\bar{\tilde{\gamma}}_{meso} = \gamma_{meso}/\Delta t$ =0.0096 s^{-1}). Solid and dashed lines correspond to $S_{\tilde{r}}$ and $S_{\delta r}$ averaged over all the particles in the sample. Dotted lines (red) correspond to exponential fits with length scales $\xi_{\tilde{r}}$=6.4 μm and $\xi_{\delta r}$ =2.5 μm.

which we find to be isotropic on the particle scale: individual particles are equally likely to have shear-induced displacements in any direction (Fig. 8). While the distributions of displacements are isotropic, this does not imply that displacements are uncorrelated spatially. To check for this, we calculate two displacement correlation functions as defined in Refs. [73–75]

$$S_{\tilde{r}}(R,\Delta t) = \frac{\langle \Delta \vec{\tilde{r}}_i \cdot \Delta \vec{\tilde{r}}_j \rangle}{\langle \Delta \tilde{r}^2 \rangle}, \qquad (6)$$

$$S_{\delta r}(R,\Delta t) = \frac{\langle \delta \tilde{r}_i \delta \tilde{r}_j \rangle}{\langle (\delta \tilde{r})^2 \rangle}, \qquad (7)$$

where the angle brackets indicate an average over all particles (see Refs. [73,75] for more details). The mobility is defined as $\delta \tilde{r} = |\Delta \tilde{r}| - \langle |\Delta \tilde{r}| \rangle$, in other words, the deviation of the magnitude of the displacement from the average magnitude of all particle displacements. The correlation functions are computed for the nonaffine displacements using Δt =45 s to maximize the "signal" (nonaffine displacements) compared to the "noise" (Brownian motion within cages on a shorter time scale).

The two correlation functions are shown in Fig. 9 for a representative data set. These functions are large at short separations R and decay for larger R, suggesting that neighboring particles are correlated in their motion. In particular, the vector-based correlation $S_{\tilde{r}}$ has a large magnitude at small R, showing neighboring particles have strongly correlated directions of motion even given that we are only considering the nonaffine displacements. The two correlation functions decay somewhat exponentially, as indicated by the straight line fits shown in Fig. 9, with decay constants $\xi_{\tilde{r}}$=6.4 μm =6.1a and $\xi_{\delta r}$=2.5 μm=2.4a (in terms of the particle radius a). The larger the slope, the more localized the correlation is. $\xi_{\tilde{r}}$ is similar to that found previously for supercooled colloidal liquids and $\xi_{\delta r}$ is slightly shorter than the prior results [73]. Overall, these results confirm that the shear-induced

particle motion is spatially heterogeneous, quite similar to what has been seen in unsheared dense liquids [43,73,75–79] and granular materials [80,81]. The length scale may be equivalent to the correlation length scale for fluidity discussed in Refs. [35,36]. For example, an experimental study of sheared polydisperse emulsions found a fluidity length scale comparable to 1–2 droplet diameters near the glass transition [35].

Considering all of our data sets, we do not find a strong dependence on either the strain rate $\dot{\gamma}$ or the total strain γ for the ranges we consider ($\bar{\dot{\gamma}}_{\mathrm{meso}}=0.006-0.02$ s^{-1}, $\gamma_{\mathrm{meso}}=0.3-1.6$). We do not have a large amount of data with which to calculate the correlation functions; unlike prior work, we cannot do a time average [73]. If we use an exponential function to fit our different data (different strains, strain rates, and volume fractions), the mobility correlation $S_{\delta r}$ yields a length scale $\xi_{\delta r}\approx 1.8-3.9$ μm and the vector correlation $S_{\vec{r}}$ yields a length scale $\xi_{\vec{r}}\approx 3.2-7.5$ μm. To check this, we also calculate

$$\xi' = \frac{\langle RS(R)\rangle}{\langle S(R)\rangle}, \tag{8}$$

where the angle brackets indicate averages over R; for a perfect exponential, we would have $\xi'=\xi$. Using this method, we find more consistent length scales of $\xi'_{\delta r}\approx(3.0-4.0)a$ and $\xi'_{\vec{r}}\approx(3.5-4.3)a$. Our data do not suggest any dependence of these length scales on the control parameters over the range we investigate. Of course, as $\dot{\gamma}\rightarrow 0$, we would expect to recover the original unstrained sample behavior [37]. Similar samples in this volume fraction range were previously found to have length scales with similar values, $\xi_{\delta r}\approx 4a-8a$ and $\xi_{\vec{r}}\approx 6a$ [73]. However, the time scales for this motion are much longer than that for our sheared samples.

C. Defining local plastic deformation

We wish to look for spatially heterogeneous dynamics, that is, how the shear-induced motion takes place locally and how particles cooperate in their motion. Several prior groups have examined local rearrangements in simulations and experiments [15,34,35,45] but have used differing ways to quantify the motion. We will discuss those quantities together and compare them using our data. We have two goals: first, to understand how different measures of local rearrangements reveal different aspects of the motion and second, to see if the spatial structure of rearranging groups of particles exhibits any particular orientation with respect to the shear direction.

For all of these definitions of rearranging groups of particles, it is useful to define a particle's nearest neighbors. Our definition of a particle's nearest neighbors is that those are the particles within the cutoff distance r_0 set by the first minimum of the pair-correlation function $g(r)$.

We start by quantifying the local strain seen by an individual particle, which is based on the average motion of its neighbors. For a particle i with center at $\vec{r}_i(t)$, the relative positions of its neighbors j are $\vec{d}_{ij}(t)=\vec{r}_j(t)-\vec{r}_i(t)$. These
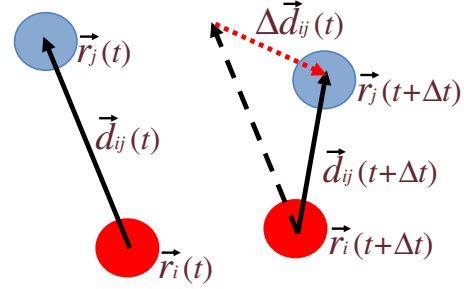

FIG. 10. (Color online) Sketch illustrating the definition of the motion of the relative position vector $\Delta\vec{d}_{ij}$ of two neighboring particles, red and blue (dark and light gray). $\vec{r}_i(t)$ represents the position of particle i at time t, $\vec{d}_{ij}(t)$ is the relative position between particles i and j at time t, and $\Delta\vec{d}_{ij}(t)$ is how the vector $\vec{d}_{ij}$ changes over the time interval $(t,t+\Delta t)$.

neighboring particles move and their motions over the next interval Δt are given by $\Delta\vec{d}_{ij}(t)=\vec{d}_{ij}(t+\Delta t)-\vec{d}_{ij}(t)$, as shown in Fig. 10.

The strain tensor $\mathbb{E}_i$ for this region around particle i is then determined by minimizing the mean squared difference between the actual relative motions $\Delta\vec{d}_{ij}(t)$ and that predicted by $\mathbb{E}_i$, in other words, choosing $\mathbb{E}_i$ to minimize

$$D^2_{i,\mathrm{min}} = \min\{\Sigma_j[\Delta\vec{d}_{ij}(t) - \mathbb{E}_i\vec{d}_{ij}(t)]^2\}. \tag{9}$$

The error, $D^2_{i,\mathrm{min}}$, quantifies the plastic deformation of the neighborhood around particle i after removing the averaged linear response $\mathbb{E}_i\vec{d}_{ij}(t)$ [34]. Thus, $D^2_{i,\mathrm{min}}$ is one way to quantify the local nonaffine rearrangement, "local" in the sense of an individual particle i and its neighbors. We term $D^2_{i,\mathrm{min}}$ the "plastic deformation." Note that the sum is computed over the ten nearest particles j to particle i, otherwise the value of $D^2_{i,\mathrm{min}}$ would depend on the number of neighbors. In practice, most of these neighboring particles are within 3.0 μm of particle i, which is comparable to the first minimum of the pair-correlation function $g(r)$, which motivates our choice of ten neighbors.

Of course, quite often $\mathbb{E}_i$ is different from the overall strain over the imaged volume, which in turn is different from the macroscopically applied strain. In practice, given that the shear is applied in x direction with the velocity gradient along z, we only treat the xz components of Eq. (9); that is, $\vec{d}_{ij}$ and $\mathbb{E}_{ij}$ can be written as

$$\vec{d}_{ij} = \begin{bmatrix} x_{ij} \\ z_{ij} \end{bmatrix}, \quad \mathbb{E}_i = \begin{bmatrix} \epsilon_i^{xx} & \epsilon_i^{xz} \\ \epsilon_i^{zx} & \epsilon_i^{zz} \end{bmatrix}. \tag{10}$$

To better understand this local strain tensor $\mathbb{E}_i$, we follow the method of Refs. [15,34]. If the particle-scale local strain was identical to the imposed strain, we would expect $\epsilon_i^{xz}=\gamma_{\mathrm{meso}}$ and the other matrix elements to be zero. We find that these expectations are true on average (for example, $\langle\epsilon_i^{xz}\rangle=\gamma_{\mathrm{meso}}$) but that for individual particles their local environment can be quite different. For each experiment, the distributions of all four matrix elements have similar standard deviations and examining different experiments, the standard deviations are between 24% and 39% of γ_{meso}.

To quantify the measured particle-scale strain, we define the "local strain"

$$\gamma_{i,\text{micro}} = \epsilon_i^{xz} + \epsilon_i^{zx} \qquad (11)$$

(using the definition of the strain tensor which is related to $\mathbb{E}$ [82]). That is, this quantity is a local approximation to the strain ($\frac{\partial u_x}{\partial z} + \frac{\partial u_z}{\partial x}$). The local strain $\gamma_{i,\text{micro}}$ is now a second way to quantify the local rearrangement of the neighborhood around particle i in addition to $D_{i,\text{min}}^2$. The diagonal elements, ϵ_i^{xx} and ϵ_i^{zz}, relate to the dilation of the local environment. In particular, the local environment stretches by a factor of $(1 + \epsilon_i^{xx})$ in the x direction and likewise $(1 + \epsilon_i^{zz})$ in the z direction. If these matrix elements are zero, then the local environment remains the same; positive matrix elements correspond to expansion and negative matrix elements correspond to contraction. We define the overall dilation as $\delta e_i = (1 + \epsilon_i^{xx})(1 + \epsilon_i^{zz}) - 1$, which is a third way to quantify the local rearrangement around particle i.

A fourth way to consider local particle motion is the previously defined nonaffine displacement, $\Delta \tilde{r}^2$. The key difference is that D_{min}^2, γ_{micro}, and δe all are derived from the actual particle motion Δr, whereas $\Delta \tilde{r}^2$ removes the motion caused by γ_{meso} [through Eq. (3)].

To demonstrate how neighboring particles rearrange and result in larger values of these various parameters, Fig. 11 shows an example using real trajectories. The original positions of the particles are shown, along with displacement vectors indicating where they move after the sample is strained with $\gamma_{\text{meso}} = 0.58$. The overall strain is seen in that particles near the top move farther than those at the bottom; however, the red (dark) particle in the middle has an unusual motion, moving downward in the $-z$ direction. Figure 11(b) shows the motion of the surrounding particles as seen in the reference frame attached to the red (dark) particle. It is these displacements that are used in the calculation Eq. (10). Figure 11(c) shows the predicted final positions of the particles (drawn large) based on $\mathbb{E}_i$, as compared to the actual final positions (drawn small); the red (dark) particle is considered "particle i." This local region experiences both shear and a strong dilation in the z direction, both captured by $\mathbb{E}_i$. The differences between the predicted and actual final positions result in a moderately large value of $D_{\text{min}}^2 = 56$ μm^2. In particular, note that D_{min}^2 is defined based on vectors pointing from the red (dark) reference particle to the other particles and because the red particle moves downward, the vectors are all greatly stretched and this increases D_{min}^2. Finally, Fig. 11(d) shows the positions of the same particles after the strain has been applied, where now the box represents the mesoscopic strain $\gamma_{\text{meso}} = 0.58$. The large spheres represent the expected positions if the motion was affine and the small spheres show the actual positions. Differences between the expected and actual positions result in large values of the nonaffine displacement $\Delta \tilde{r}$. For the red (dark) particle, $\Delta \tilde{r} = 2.97$ μm. Overall, the anomalous motion of the central particle i is because under the large local strain, this particle makes a large jump out of its original cage. It is these sorts of unusual motions that result in large plastic deformations within the sample.
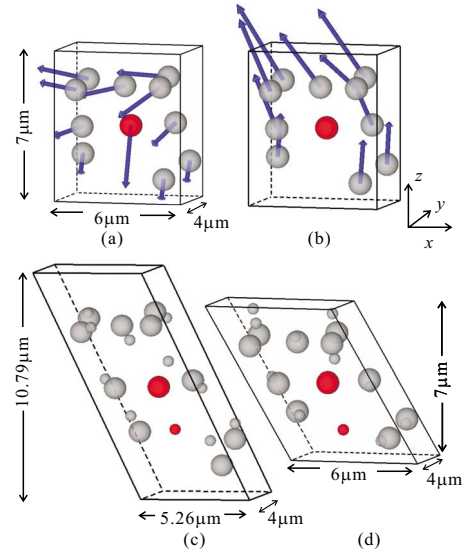

FIG. 11. (Color online) These four sketches show different portrayals of a particle with unusual motion. (a) Particle motion as seen in the laboratory reference frame. Arrows indicate displacement vectors. (b) Similar to (a) except the motion are in the reference frame where the central red (darker) particle is motionless. (c) Large spheres correspond to the expected positions of the particles and the smaller spheres correspond to the actual positions of the particles. The distortion of the box and the expected positions of the particles are calculated based on the measured local strain tensor $\mathbb{E}_i$, where red (darker) particle is particle i. For this local neighborhood, we have $\gamma_{\text{micro}} = 0.73$ and a dilation primarily in the z direction ($\epsilon^{xx} = -0.1$, $\epsilon^{zz} = 0.5$, and $\delta e = 0.35$). (d) The positions of the same particles after the strain has been applied, where now the box represents the mesoscopic strain $\gamma_{\text{meso}} = 0.58$. The large spheres represent the expected positions if the motion was affine and the small spheres show the actual positions. For all panels, to show the displacements in three dimensions better, the radii of the large spheres are 0.5 of the real scale. Data correspond to a sample with $\phi = 0.51$, $\gamma_{\text{meso}} = 0.58$, $\bar{\dot{\gamma}}_{\text{meso}} = 0.014$ s^{-1}, and $\Delta t = 40$ s.

D. Collective particle motions

To investigate the relationships between these quantities, a 3-μm-thin y slice of a sample with volume fraction $\phi = 0.51$ is shown in several ways in Fig. 12. In panel (a), the x displacement is shown, making the strain apparent. Panel (b) shows the original Voronoi volumes for each particle at $t = 0$. The Voronoi cell for each particle is defined as the volume closer to the center of that particle than to any other particle. In subsequent panels, the darker colors indicate larger local rearrangements, as measured by the nonaffine displacement $\Delta \tilde{r}^2$ [panel (c)], plastic deformation D_{min}^2 [panel (d)], local strain γ_{micro} [panel (e)], and dilation δe [panel (f)]. It can be seen that the darker-colored particles cluster together, indicating that for each of these measures of local rearrangement, the motions are spatially heterogeneous [15]. This is a real-space picture showing conceptually what is indicated by the correlation functions in Fig. 9 that neighboring particles have similar motions. These pictures are qualitatively similar to those seen for thermally induced cage rearrangements in supercooled liquids [43,77,78,83,84] and
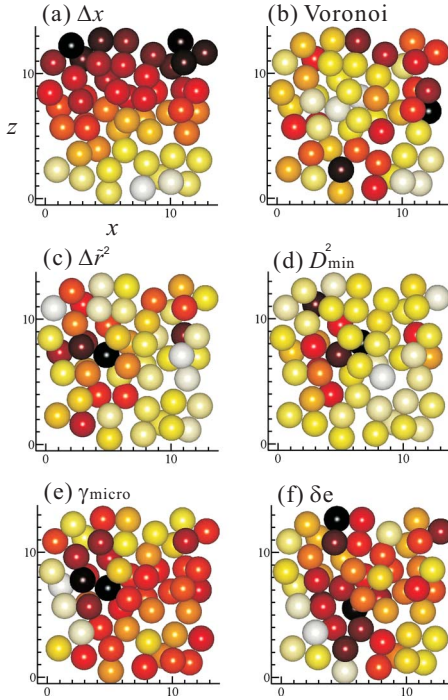
FIG. 12. (Color online) A 3-μm-thin cut through the sample, showing the xz shear plane; axes are as labeled in (a). The particles are drawn in their location at $t=0$, the start of this strain half cycle. (a) Darker particles have larger values of Δx, thus indicating the applied strain. The top particles (large z) are moving left (dark colors) and the bottom particles are moving right (light colors). (b) Darker particles have larger Voronoi volumes at $t=0$. (c) Darker particles have larger values of the nonaffine motion $\Delta \tilde{r}^2$. (d) Darker particles have larger values of the plastic deformation $D_{\min}^2$. (e) Darker particles have larger values of the local strain γ_{micro}. (f) Darker particles have larger values of the dilation δe. The sample is the same as the data shown in Fig. 5 (see that figure caption for details).

glasses [81,85–88]. Furthermore, by comparing these images, it is apparent that particles often have large values of several quantities simultaneously; in particular, compare panels (c) and (d), and panels (e) and (f). While the correspondence is not exact, it suggests that all four of these ideas are capturing similar features of rearranging regions. However, it is also clear that there are differences between (c) and (d) as compared to (e) and (f). In the latter two panels, the region of high activity is spread out over a larger area; more of the particles are deforming by these measures at the same time. Nonetheless, in all four cases, the particles around $x \approx 2-4$ μm are experiencing the most extreme deformations.

The Voronoi volume [Fig. 12(b)] has previously been found to be slightly correlated with particle motion in unsheared colloidal supercooled liquids [68,89]; that is, particles with large Voronoi volumes have space to move and thus are likely to have larger displacements than average. Here it appears that there is no correlation between the Voronoi volume and the particle motion, suggesting that for these strained samples, the local volume is not a crucial influence on the motion [38]. This is probably because in the end, all cages must rearrange for the strain to occur.
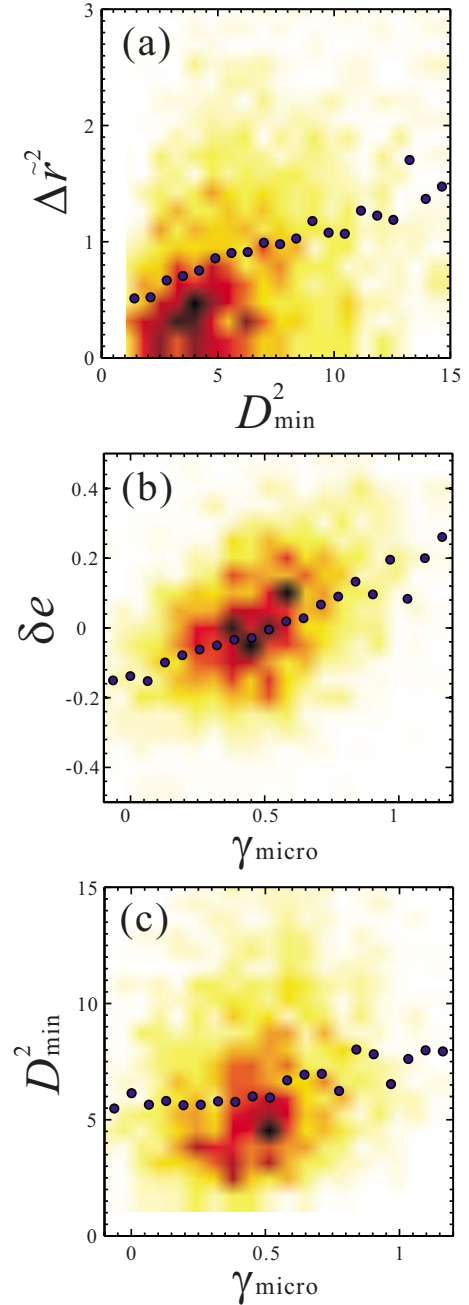

FIG. 13. (Color online) 2D histograms of (a) $D_{\min}^2$ and $\Delta \tilde{r}^2$, (b) γ_{micro} vs dilation δe, and (c) γ_{micro} and $D_{\min}^2$. The sample has the same parameters as Fig. 5 (see that caption for details). In these histograms, darker colors stand for the larger probability. Dotted lines are the average values of the y axis corresponding to each value on the x axis. The correlation coefficients between each pair of variables are (a) $C=0.43\pm0.11$, (b) $C=0.42\pm0.09$, and (c) $C=0.17\pm0.05$ (see text for details).

To demonstrate the relationships between the measures of plastic deformation more quantitatively, we compute two-dimensional (2D) histograms comparing pairs of the variables, shown in Fig. 13. The darker color indicates larger joint probability and the dotted line represents the mean value of the quantity on the vertical axis corresponding to the quantity on the horizontal axis. Figure 13(a) shows that on

average, particles with a large plastic deformation D_{min}^2 are also much likelier to have a large nonaffine displacement $\Delta \tilde{r}^2$. This is suggested by the specific example shown in Figs. 11(c) and 11(d). Similarly, Fig. 13(b) shows that a particle's microscopic strain γ_{micro} is well correlated with the dilation δe. For these data, the mesoscopic strain is $\gamma_{meso} = 0.43$; particles with $\gamma_{micro} < \gamma_{meso}$ are more often in local environments that contract ($\delta e < 0$) and vice versa. As a contrast, Fig. 13(c) shows a somewhat weaker correlation between D_{min}^2 and γ_{micro}. The Pearson correlation coefficients between these quantities are $C(D_{min}^2, \Delta \tilde{r}^2) = 0.43 \pm 0.11$, $C(\gamma_{micro}, \delta e) = 0.42 \pm 0.09$, and $C(\gamma_{micro}, D_{min}^2) = 0.17 \pm 0.05$. The uncertainties are from the standard deviations of the correlation coefficients from the nine different experiments we conducted.

Overall, Fig. 13 suggests that D_{min}^2 and $\Delta \tilde{r}^2$ both capture the idea of plastic deformation [66]. The correspondence between these two variables is nontrivial, given that $\Delta \tilde{r}^2$ is based on trajectories with the overall strain removed (the strain computed from all observed particles), whereas D_{min}^2 only accounts for the very localized strain of the neighboring particles. In contrast, γ_{micro} and δe are well suited to examine particles moving in atypical ways; typical particles have $\gamma_{micro} \approx \gamma_{meso}$ and $\delta e = 0$. These two separate ideas (plastic deformation and atypicality) are only weakly correlated. Other than the three specific comparisons shown in Fig. 13, all other comparisons are even less correlated ($|C| < 0.1$). We also examined the quantities $|\gamma_{micro} - \gamma_{meso}|$ and $|\delta e|$ as ways to measure the deviations from typical behavior; these quantities are also only weakly correlated with the other measures of deformation.

We now return to the question of the isotropy of the motion. Figure 8 indicates that the distribution of all particle motions is isotropic, but it is possible that the spatially heterogeneous groups of highly mobile particles shown in Fig. 12 are themselves oriented along a preferred direction. To investigate the 3D structures of these relaxation regions, we quantify the sizes of these active regions in the x, y, and z directions. To start, we define connected neighboring particles as those with separations less than r_0, the distance where pair-correlation function $g(r)$ reaches its first minimum. [Note that this is slightly different from the neighbor definition used for Eq. (9); see the discussion following that equation.] For a given quantity, we consider active particles as those in the top 20% of that quantity, similar to prior work [37,43,77,85]. We then define the active region as a cluster of connected active particles. For example, Fig. 14 shows a cluster of particles with large nonaffine displacements [panel (a)] and a cluster with large plastic deformations [panel (b)]. Each cluster is drawn from the same data set and the particles drawn in red (darker) are common to both clusters. [Note that clusters drawn based on γ_{micro} and δe are smaller. In Figs. 12(e) and 12(f), more regions have large values of these parameters, but the top 20% most active are not clustered to the extent they are in Figs. 12(c) and 12(d).]

We wish to understand if the shapes of such clusters show a bias along any particular direction. It is important that the experimental observation volume not bias the result, so from within the observed 3D volume, we consider only particles that start within an isotropic cube of dimensions 15×15

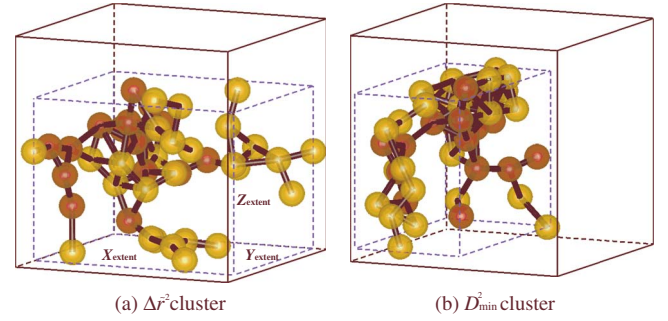(a) $\Delta \tilde{r}^2$ cluster   (b) D_{min}^2 cluster

FIG. 14. (Color online) Cluster of neighboring particles with large values of (a) nonaffine motion $\Delta \tilde{r}^2$ and (b) plastic deformation D_{min}^2. To avoid biasing the cluster shape, the particles are drawn from within a $15 \times 15 \times 15$ μm^3 cube (solid lines). Dashed lines indicate the spatial extent of the two cluster shapes in each direction. The cluster in (a) is $14 \times 12 \times 11$ μm^3 and the cluster in (b) is $8 \times 14 \times 10$ μm^3. Red particles are common between the two clusters and the black bonds indicate neighboring particles; particle sizes are drawn 0.8 times the actual scale to make the connections more visible. In each case, the particles shown are the top 20% for the parameter chosen. Data corresponds to the same parameters as in Fig. 5 (see that caption for details).

$\times 15$ μm^3. The size of this cube is chosen to be the largest cube for which all the particles are within the optical field of view for the full half cycle of shear for all experiments. (See the related discussion at the end of Sec. II). Within this isotropic volume, we consider the largest cluster from each experiment and for each considered variable. We then define the extent of that cluster in each direction from the positions of each particle within the cluster as $x_{extent} = \max(x_i) - \min(x_i)$ and similarly for y and z.

Anisotropic cluster shapes would be manifested by systematic differences in the relative magnitudes of x_{extent}, y_{extent}, and z_{extent}. We compare these in Fig. 15 for clusters of particles with large nonaffine motion $\Delta \tilde{r}^2$ [panel (a)] and large plastic deformation D_{min}^2 [panel (b)]. The comparison is made by using the ratios y_{extent}/x_{extent} and z_{extent}/x_{extent}, thus normalizing the extent in the y and z directions by that of the shear velocity direction x. Thus, if a cluster has the same extent in x and y, y_{extent}/x_{extent} should be equal to 1, along the vertical dashed line. Similarly, for the same extent in x and z, points should be along the horizontal dashed line with $z_{extent}/x_{extent} = 1$. If the extent is the same for y and z, the points should be along the diagonal line with $y_{extent}/x_{extent} = z_{extent}/x_{extent}$. For an isotropic cluster with same size in all dimensions, the point should be in the center (1,1).

As shown in Fig. 15, for all of our data, we find no systematic anisotropy; the cluster extent ratios are mostly clustered around the isotropic point (1,1). Due to random fluctuations, no cluster is perfectly isotropic, yet the points seem fairly evenly distributed around the three dashed lines. Thus, while the shear-induced rearrangements take place in localized regions (Fig. 12), data indicate that these regions on average have no directional bias. This seems true for both the nonaffine displacements $\Delta \tilde{r}^2$ in Fig. 15(a) and the plastic deformation D_{min}^2 in Fig. 15(b).
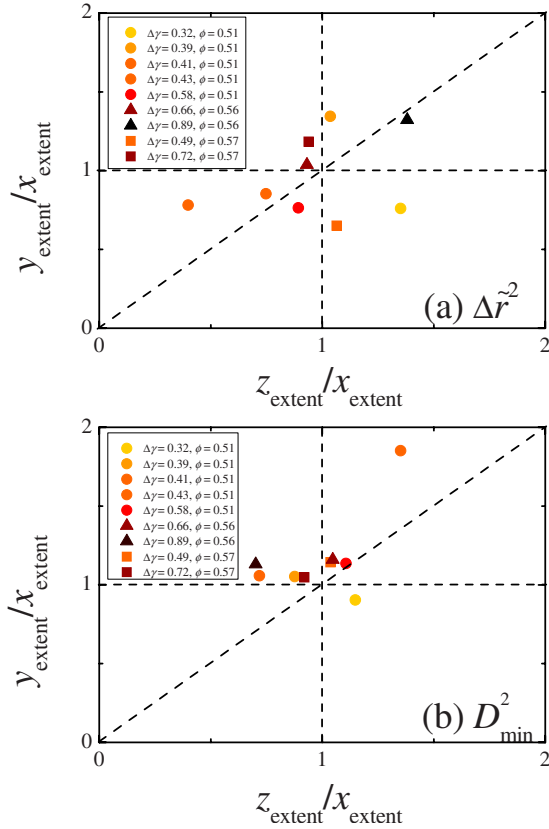
FIG. 15. (Color online) Comparison between the cluster extent in x, y, and z based on different variables. (a) Particles with the largest nonaffine motion $\Delta \tilde{r}$. (b) Particles with the largest plastic deformation D_{min}^2. Symbols represent different volume fractions: $\phi = 0.51$ (circles), 0.56 (triangles), and 0.57 (squares). Colors (or grays from light to dark) represent different accumulative strains $\gamma_{meso} = 0.3-0.9$. The clusters are comprised of the top 20% of the particles with the given characteristic.

IV. DISCUSSION

We examined the microscopic plastic deformations occurring in several sheared dense colloidal suspensions. Our first main observation is that on average, individual particles have no bias in their direction of motion other than that trivially imposed by the strain. When this imposed motion is removed from the particle trajectories, the remaining shear-induced motion is isotropic: particles are equally likely to move in any direction. Our second main observation is on the shape of groups of particles undergoing plastic rearrangements. There are several ways to determine which particles are rearranging and we have shown that all of these are useful for highlighting local regions of deformation. Furthermore, the shapes of these regions are also isotropic. However, we cannot rule out that with more data and subtler analysis, we might find anisotropies in particle motion [90].

In our results, we find little dependence on the overall volume fraction ϕ, total strain, or strain rate. For the volume fraction, all of our samples are dense liquids with $\phi < \phi_G$. At significantly lower volume fractions, presumably particles would not be caged and the shear-induced rearrangements might be quite different [70]. At higher volume fractions $\phi > \phi_G$, prior work has seen similar results [15,39] although not examined the shapes of the rearranging regions in detail. It is possible that results in glassy samples might be different given that near ϕ_G, slight changes in volume fraction have large consequences [42], but we have not seen clear evidence of that in our data. For the total strain, we have not examined a wide range of parameters. In all cases, we are studying sufficiently large enough strains to induce irreversible, plastic rearrangements. For the strain rates, all of our strain rates are fast enough such that the modified Peclet number Pe* is at least 7, so that thermally induced diffusive motion is less relevant. It is likely that at slower strain rates (lower Peclet numbers), different behavior would be seen [37].

Previous work [54,91–93] found that oscillatory shear can induce crystallization of concentrated colloidal suspensions. The "induction time" of this crystallization is strain dependent: a larger strain amplitude results in shorter induction time. In our experiments, we studied only a limited number of oscillations and our strain amplitude ~ 1. We did not observe crystallization in any of our experiments. It is likely that were we to continue our observations for much longer times, we could see the onset of shear-induced crystallization and so we note that our experiments are probably studying a nonequilibrium state. Additionally, Fig. 4 shows that our strain rate takes a while to stabilize after flow reversal, which again suggests that our results are not in steady state. Thus, it is possible that our primary observation, that the shear-induced particle rearrangements are isotropic in character, is limited only to the transient regime we observe. It is still intriguing that in this regime, particle motion is so isotropic. For example, Fig. 4 shows that the sample takes a while to requilibrate after shear reversal, yet there is no obvious signature of this in the particle motion or the configurations of the particles. Likewise, presumably the long-term crystallization will be caused by anisotropic motion (and result in further anisotropic motion), but no signs of this are present in the early-time amorphous samples we study. It would be interesting to conduct longer-term experiments to relate the particle rearrangements to those resulting in crystallization. Alternatively, it would be also interesting to use a cone-and-plate geometry shear cell capable of indefinitely large strains [62] to reach the steady-state constant shear regime.

[1] C. A. Angell, K. L. Ngai, G. B. McKenna, P. F. McMillan, and S. W. Martin, J. Appl. Phys. **88**, 3113 (2000).

[2] P. Coussot and F. Gaulard, Phys. Rev. E **72**, 031409 (2005).

[3] J. Ubbink, A. Burbidge, and R. Mezzenga, Soft Matter **4**, 1569 (2008).

[4] R. Mezzenga, P. Schurtenberger, A. Burbidge, and M. Michel, Nature Mater. **4**, 729 (2005).

[5] A. J. Liu and S. R. Nagel, Nature (London) **396**, 21 (1998).

[6] P. Coussot, J. S. Raynaud, F. Bertrand, P. Moucheront, J. P. Guilbaud, H. T. Huynh, S. Jarny, and D. Lesueur, Phys. Rev. Lett. **88**, 218301 (2002).

[7] N. Huang, G. Ovarlez, F. Bertrand, S. Rodts, P. Coussot, and D. Bonn, Phys. Rev. Lett. **94**, 028301 (2005).

[8] F. S. Merkt, R. D. Deegan, D. I. Goldman, E. C. Rericha, and H. L. Swinney, Phys. Rev. Lett. **92**, 184501 (2004).

[9] F. Spaepen, Acta Metall. **25**, 407 (1977).

[10] H. W. Sheng, H. Z. Liu, Y. Q. Cheng, J. Wen, P. L. Lee, W. K. Luo, S. D. Shastri, and E. Ma, Nature Mater. **6**, 192 (2007).

[11] C. A. Schuh, T. C. Hufnagel, and U. Ramamurty, Acta Mater. **55**, 4067 (2007).

[12] P. N. Pusey and W. van Megen, Nature (London) **320**, 340 (1986).

[13] M. D. Haw, J. Phys.: Condens. Matter **14**, 7769 (2002).

[14] S. Suresh, Nature Mater. **5**, 253 (2006).

[15] P. Schall, D. A. Weitz, and F. Spaepen, Science **318**, 1895 (2007).

[16] P. Habdas and E. R. Weeks, Curr. Opin. Colloid Interface Sci. **7**, 196 (2002).

[17] V. Prasad, D. Semwogerere, and E. R. Weeks, J. Phys.: Condens. Matter **19**, 113102 (2007).

[18] M. S. Elliot and W. C. K. Poon, Adv. Colloid Interface Sci. **92**, 133 (2001).

[19] W. van Megen and P. N. Pusey, Phys. Rev. A **43**, 5429 (1991).

[20] R. J. Speedy, Mol. Phys. **95**, 169 (1998).

[21] G. Brambilla, D. El Masri, M. Pierno, L. Berthier, L. Cipelletti, G. Petekidis, and A. B. Schofield, Phys. Rev. Lett. **102**, 085703 (2009).

[22] C. S. O'Hern, L. E. Silbert, A. J. Liu, and S. R. Nagel, Phys. Rev. E **68**, 011306 (2003).

[23] J. D. Bernal, Proc. R. Soc. London, Ser. A **280**, 299 (1964).

[24] S. Torquato, T. M. Truskett, and P. G. Debenedetti, Phys. Rev. Lett. **84**, 2064 (2000).

[25] A. Donev, S. Torquato, F. H. Stillinger, and R. Connelly, Phys. Rev. E **70**, 043301 (2004).

[26] C. S. O'Hern, L. E. Silbert, A. J. Liu, and S. R. Nagel, Phys. Rev. E **70**, 043302 (2004).

[27] A. van Blaaderen and P. Wiltzius, Science **270**, 1177 (1995).

[28] W. van Megen and S. M. Underwood, Phys. Rev. E **47**, 248 (1993).

[29] W. van Megen and S. M. Underwood, Phys. Rev. E **49**, 4206 (1994).

[30] I. Snook, W. van Megen, and P. Pusey, Phys. Rev. A **43**, 6900 (1991).

[31] E. Bartsch, V. Frenz, S. Moller, and H. Sillescu, Physica A **201**, 363 (1993).

[32] E. Bartsch, J. Non-Cryst. Solids **192-193**, 384 (1995).

[33] T. G. Mason and D. A. Weitz, Phys. Rev. Lett. **75**, 2770 (1995).

[34] M. L. Falk and J. S. Langer, Phys. Rev. E **57**, 7192 (1998).

[35] J. Goyon, A. Colin, G. Ovarlez, A. Ajdari, and L. Bocquet, Nature (London) **454**, 84 (2008).

[36] L. Bocquet, A. Colin, and A. Ajdari, Phys. Rev. Lett. **103**, 036001 (2009).

[37] R. Yamamoto and A. Onuki, Europhys. Lett. **40**, 61 (1997).

[38] K. Miyazaki, D. R. Reichman, and R. Yamamoto, Phys. Rev. E **70**, 011501 (2004).

[39] R. Besseling, E. R. Weeks, A. B. Schofield, and W. C. K. Poon, Phys. Rev. Lett. **99**, 028301 (2007).

[40] K. Maeda and S. Takeuchi, Philos. Mag. A **44**, 643 (1981).

[41] Y. Shi and M. L. Falk, Phys. Rev. Lett. **95**, 095502 (2005).

[42] Z. Cheng, J. Zhu, P. M. Chaikin, S.-E. Phan, and W. B. Russel, Phys. Rev. E **65**, 041405 (2002).

[43] E. R. Weeks, J. C. Crocker, A. C. Levitt, A. Schofield, and D. A. Weitz, Science **287**, 627 (2000).

[44] Y. Wang, K. Krishan, and M. Dennin, Phys. Rev. E **74**, 041405 (2006).

[45] B. Utter and R. P. Behringer, Phys. Rev. Lett. **100**, 208302 (2008).

[46] G. Petekidis, A. Moussaïd, and P. N. Pusey, Phys. Rev. E **66**, 051402 (2002).

[47] L. Antl, J. W. Goodwin, R. D. Hill, R. H. Ottewill, S. M. Owens, S. Papworth, and J. A. Waters, Colloids Surf. **17**, 67 (1986).

[48] A. D. Dinsmore, E. R. Weeks, V. Prasad, A. C. Levitt, and D. A. Weitz, Appl. Opt. **40**, 4152 (2001).

[49] S. Auer and D. Frenkel, Nature (London) **413**, 711 (2001).

[50] S. I. Henderson, T. C. Mortensen, S. M. Underwood, and W. van Megen, Physica A **233**, 102 (1996).

[51] H. J. Schöpe, G. Bryant, and W. van Megen, J. Chem. Phys. **127**, 084505 (2007).

[52] U. Gasser, E. R. Weeks, A. Schofield, P. N. Pusey, and D. A. Weitz, Science **292**, 258 (2001).

[53] J. Hernández-Guzmán and E. R. Weeks, Proc. Natl. Acad. Sci. U.S.A. **106**, 15198 (2009).

[54] M. D. Haw, W. C. K. Poon, and P. N. Pusey, Phys. Rev. E **57**, 6859 (1998).

[55] N. Duff and D. J. Lacks, Phys. Rev. E **75**, 031501 (2007).

[56] R. P. A. Dullens, D. G. A. L. Aarts, and W. K. Kegel, Phys. Rev. Lett. **97**, 228301 (2006).

[57] P. R. ten Wolde, M. J. Ruiz-Montero, and D. Frenkel, J. Chem. Phys. **104**, 9932 (1996).

[58] P. J. Steinhardt, D. R. Nelson, and M. Ronchetti, Phys. Rev. B **28**, 784 (1983).

[59] A. van Blaaderen, A. Imhof, W. Hage, and A. Vrij, Langmuir **8**, 1514 (1992).

[60] L. T. Shereda, R. G. Larson, and M. J. Solomon, Phys. Rev. Lett. **101**, 038301 (2008).

[61] J. C. Crocker and D. G. Grier, J. Colloid Interface Sci. **179**, 298 (1996).

[62] R. Besseling, L. Isa, E. Weeks, and W. Poon, Adv. Colloid Interface Sci. **146**, 1 (2009).

[63] C.-L. Chan, W.-Y. Woon, and L. I, Phys. Rev. Lett. **93**, 220602 (2004).

[64] J. Lauridsen, G. Chanan, and M. Dennin, Phys. Rev. Lett. **93**, 018303 (2004).

[65] I. Cohen, B. Davidovitch, A. B. Schofield, M. P. Brenner, and D. A. Weitz, Phys. Rev. Lett. **97**, 215502 (2006).

[66] A. Lemaître and C. Caroli, Phys. Rev. E **76**, 036104 (2007).

[67] C. E. Maloney and M. O. Robbins, J. Phys.: Condens. Matter **20**, 244128 (2008).

[68] E. R. Weeks and D. A. Weitz, Phys. Rev. Lett. **89**, 095704 (2002).

[69] F. Delogu, Phys. Rev. Lett. **100**, 075901 (2008).

[70] D. J. Pine, J. P. Gollub, J. F. Brady, and A. M. Leshansky, Nature (London) **438**, 997 (2005).

[71] C. Eisenmann, C. Kim, J. Mattsson, and D. A. Weitz (unpublished).

[72] A. Tanguy, F. Leonforte, and J. L. Barrat, Eur. Phys. J. E **20**, 355 (2006).

[73] E. R. Weeks, J. C. Crocker, and D. A. Weitz, J. Phys.: Condens. Matter **19**, 205131 (2007).

[74] J. C. Crocker, M. T. Valentine, E. R. Weeks, T. Gisler, P. D. Kaplan, A. G. Yodh, and D. A. Weitz, Phys. Rev. Lett. **85**, 888 (2000).

[75] B. Doliwa and A. Heuer, Phys. Rev. E **61**, 6898 (2000).

[76] M. D. Ediger, C. A. Angell, and S. R. Nagel, J. Phys. Chem. **100**, 13200 (1996).

[77] C. Donati, J. F. Douglas, W. Kob, S. J. Plimpton, P. H. Poole, and S. C. Glotzer, Phys. Rev. Lett. **80**, 2338 (1998).

[78] W. K. Kegel and A. van Blaaderen, Science **287**, 290 (2000).

[79] M. D. Ediger, Annu. Rev. Phys. Chem. **51**, 99 (2000).

[80] A. Mehta, G. C. Barker, and J. M. Luck, Proc. Natl. Acad. Sci. U.S.A. **105**, 8244 (2008).

[81] D. I. Goldman and H. L. Swinney, Phys. Rev. Lett. **96**, 145702 (2006).

[82] L. D. Landau and E. M. Lifshitz, *Theory of Elasticity, Course of Theoretical Physics*, 3rd ed. (Elsevier, Oxford, UK, 1986), Vol. 7, Chap. 1.

[83] R. Yamamoto and A. Onuki, Phys. Rev. Lett. **81**, 4915 (1998).

[84] L. Berthier, Phys. Rev. E **69**, 020201(R) (2004).

[85] R. E. Courtland and E. R. Weeks, J. Phys.: Condens. Matter **15**, 359 (2003).

[86] K. Vollmayr-Lee, W. Kob, K. Binder, and A. Zippelius, J. Chem. Phys. **116**, 5158 (2002).

[87] J. D. Stevenson, J. Schmalian, and P. G. Wolynes, Nat. Phys. **2**, 268 (2006).

[88] T. Kawasaki, T. Araki, and H. Tanaka, Phys. Rev. Lett. **99**, 215701 (2007).

[89] J. C. Conrad, P. P. Dhillon, E. R. Weeks, D. R. Reichman, and D. A. Weitz, Phys. Rev. Lett. **97**, 265701 (2006).

[90] A. Furukawa, K. Kim, S. Saito, and H. Tanaka, Phys. Rev. Lett. **102**, 016001 (2009).

[91] B. J. Ackerson and P. N. Pusey, Phys. Rev. Lett. **61**, 1033 (1988).

[92] B. J. Ackerson, J. Phys.: Condens. Matter **2**, 389 (1990).

[93] M. D. Haw, W. C. K. Poon, P. N. Pusey, P. Hebraud, and F. Lequeux, Phys. Rev. E **58**, 4673 (1998).